INTERNATIONAL JOURNAL FOR NUMERICAL METHODS IN FLUIDS
Int. J. Numer. Meth. Fluids 2008; **57**:495–517
Published online 8 November 2007 in Wiley InterScience (www.interscience.wiley.com). DOI: 10.1002/fld.1642

Reconstruction of shape and its effect on flow in arterial conduits

A. M. Gambaruto[1], J. Peiró[1,*,†], Denis J. Doorly[1] and A. G. Radaelli[1,2]

[1]*Department of Aeronautics, Imperial College London, South Kensington Campus, London SW7 2AZ, U.K.*
[2]*Computational Imaging Lab, Information and Communication Technologies Department, Universitat Pompeu Fabra, Passeig de Circumval.lació 8, E08003 Barcelona, Spain*

SUMMARY

The geometry of arterial conduits derived from *in vivo* image data is subject to acquisition and reconstruction errors. This results in a degree of uncertainty in defining the bounding geometry for a patient-specific anatomical conduit. In applying computational fluid dynamics to model the flow in specific anatomical configurations, the effect of the uncertainty in boundary definition should be considered, particularly if the objective is to extract quantitative measures of the local haemodynamics.

Taking an example of a bypass graft configuration, we examine the effects of image threshold, surface smoothing and semi-idealization on the modelled geometry and the resulting flow. Procedures for reconstruction from medical images are outlined and applied with different parameter values within the image uncertainty range to create alternative models from the same data set.

Methods to characterize the flow structure and wall shear stress (WSS) are introduced and used to provide quantitative comparison of the different haemodynamic environments associated with the varying model geometries. Comparable effects on the WSS distribution are found to occur with progressively increased surface smoothing and semi-idealization of the geometry by elliptical section fitting. Significant differences in WSS correspond to different threshold choices. Copyright © 2007 John Wiley & Sons, Ltd.

Received 11 May 2007; Revised 19 September 2007; Accepted 20 September 2007

KEY WORDS: shape reconstruction; medical image processing; surface smoothing; segmentation uncertainty; topology idealization, sensitivity and confidence bounds

1. INTRODUCTION

Most cardiovascular diseases are associated with an abnormal biological response caused by unusual haemodynamic conditions [1]. One manifestation of cardiovascular disease is in the peripheral arteries, termed *peripheral arterial disease* (PAD) [2]. PAD arises through atherogenesis,

*Correspondence to: J. Peiró, Department of Aeronautics, Imperial College London, South Kensington Campus, London SW7 2AZ, U.K.
†E-mail: j.peiro@imperial.ac.uk

Contract/grant sponsor: EU; contract/grant number: HPRN-CT-2002-00270

affecting a large number of people in the western world. It may manifest itself as intermittent claudication but may lead more alarmingly to amputation or even mortality [3].

It has been postulated since the work of [4] that atheroma in man is predisposed to occur in regions of low *wall shear stress* (WSS), while being inhibited or retarded in regions of high WSS. Furthermore, most intimal thickening is found in regions where the average WSS is less than 1.0 Pa (10 dynes/cm^2) [1]. On the other hand, an upper limit to the safe value of WSS is proposed as 37.9 Pa [5] which is physiologically difficult to achieve. Other measures related to the WSS (e.g. the oscillatory shear index) have been studied, and whereas there is a considerable discussion as to which measure correlates best with disease occurrence, it is generally accepted that low values of WSS are undesirable [6, 7]. In this work the WSS will be taken as the primary measure of the vessel haemodynamics and used to assess the sensitivity of the computed flow to the geometric definition.

The curvature and branching of arteries means that a non-uniform distribution of WSS is inevitable, but at any location, the degree and pattern of non-uniformity depends on both global and local features of the specific flow conduit topology. Furthermore, for any specific anatomical region, the relevant conduit geometry varies significantly from one person to the next, in normal let alone pathological subjects, with corresponding implications for the haemodynamic conditions. This is discussed by Younis *et al*. [8], who considered inter-individual variations in flow and wall mechanics in the region of the carotid artery bifurcation. The issue of how to classify topological variations in arterial anatomy and the consequences for flow is a topic that is as yet hardly explored. Apart from natural differences between individuals, variations in geometry produced through surgical intervention may also have profound consequences; in the context of bypass grafts, Giordana *et al*. [9, 10] employ the mean orientation angles of principal vascular segments at an anastomosis as a global measure, and the respective cross-sectional area variations as local measures in describing different bypass configurations.

The variation in arterial haemodynamics consequent on anatomical variations thus calls for modelling to be patient specific. Tomographic imaging *in vivo* has provided an essential enabling step, and modelling procedures in which the arterial geometry is determined are reviewed in [11, 12]. Several detailed expositions of particular techniques exist, one such is the work of Antiga *et al*. [13]; this work also highlights the need for user intervention in defining the bounding geometry.

Despite the growing focus on patient-specific studies, little attempt has yet been made to quantify the modelling uncertainty. Some attention has been given to this topic, with Löhner *et al*. [12] raising the issue; however, they do not present quantitative results. A sensitivity analysis of flow in cerebral aneurisms was performed by Cebral *et al*. [14], revealing the strong influence of the geometry on the flow. Their findings serve to emphasize the need to investigate solution sensitivity in the presence of modelling uncertainty.

In general, errors and uncertainty in modelling the haemodynamics from *in vivo*-acquired data can be categorized according to where they appear in the following four stages: (1) errors in the biophysical basis of the complete model (for example, neglect of phenomena such as wall compliance and complex blood rheology); (2) *in vivo* errors in the measurement data, including systematic errors such as image acquisition distortions and inflow rate errors (for example, due to incorrect Doppler ultrasound positioning), and errors in other data required as parameter values for the numerical models; (3) the propagation of second-stage errors by the transformation of measured data to build a model, including errors in the transformation procedures themselves, (with both forms of error occurring in the reconstruction of geometry from medical images);

DOI: 10.1002/fld

and (4) errors in numerical solution. Although the overall error is compounded in a non-linear manner by each of the above components, it is useful to examine how they affect the solution individually.

In this work, flow solutions are obtained under restrictive assumptions (laminar flow of a Newtonian fluid and without fluid–structure interaction), for which the numerical procedures used are well validated; errors at the fourth stage are thus not considered here. Examples of work that addresses systematic errors in the second stage are [15] in which image artefacts due to flow features are investigated; Steinman [11] addresses the third stage. Errors in defining the biophysical basis of models at the first stage are more difficult to quantify. One approach is to compare results obtained from simple models, with those in which some assumptions are relaxed, for example, where wall motion is allowed [8]. Clearly, it is desirable to compare modelled results with detailed *in vivo* flow measurements, although the capability of current combined non-invasive measurement and imaging techniques presently limits the availability of such data.

Here we consider only the effects of errors during the third stage, specifically the consequences of uncertainty in geometric definition arising through the reconstruction process. Although the image quality may be variable, it is assumed to be devoid of distortion artefacts; likewise we ignore errors in specifying the inflow boundary conditions. Ascribing greater precedence to errors in geometry than errors in specifying the inflow conditions appears to be justified for initial work such as this. For example, the study of flow in a human right coronary artery of Meyers *et al.* [16] found the inflow conditions to be of secondary importance to the geometry. As the flow must respond both to continuous changes in geometry, and to viscous diffusion from the wall, inflow effects are bound to diminish with distance so that finding is not unexpected. Conversely, over short distances determination of the velocity profile at inflow is essential, whilst for unsteady simulations the pulse waveform must be well specified.

Errors in the reconstruction procedure are caused predominantly by noise and artefacts associated with imaging errors [17–19]. For example, magnetic resonance (MR) imaging of vascular geometries is gaining popularity, but is often subject to artefacts such as those shown in Figure 1. Even in the absence of such artefacts, different automatic medical image segmentation and virtual model reconstruction schemes also introduce variability in the geometry.

Previous studies have mostly been based on simple, quasi-circular vessels, but they show that artefacts in the reconstruction can bring about variations in the geometry that may lead to different conclusions regarding the haemodynamic environment. Smoothing of the geometry has been found to be associated with a reduction of the effects of these artefacts. However, the extent of smoothing that should be performed and the degree of geometric alteration produced by smoothing has not generally been considered.

There is therefore a lack of information on the impact of geometric differences incurred in the reconstruction procedure on the resultant flow solution and it is this aspect of the sensitivity analysis that we will consider in this work. How to quantify these and thus obtain a measure of the uncertainty when performing a patient-specific study is clearly desirable. One possible approach to determine the sensitivity of the flow would be to formulate a set of variables which define the perturbations to the boundary conditions; a comprehensive assessment of the probabilistic range of flow outcomes for a pre-supposed distribution of perturbation parameters could in principle be determined. However, before undertaking such computationally intensive studies, we consider it sensible to perform a limited investigation, in order to: indicate appropriate ranges of parameter values, determine the consequent degree of variation in the flow, and explore means to assess the

DOI: 10.1002/fld

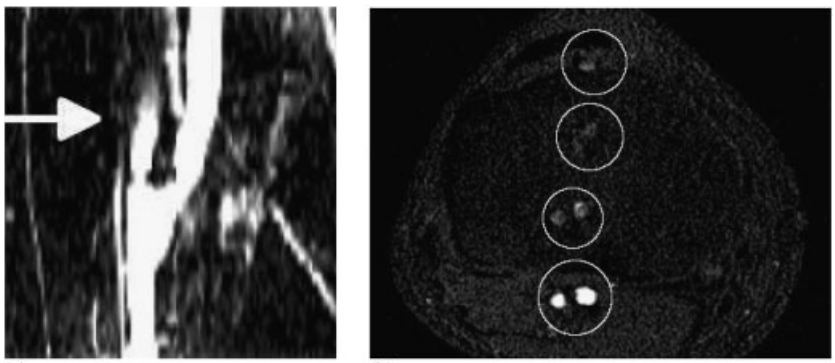

Figure 1. Examples of artefacts in MR imaging for the bypass graft geometry used in this work. (a) Maximum intensity projection of the anastomosis. The arrow indicates a proximal vessel disappearing in the proximal direction. (b) Ghosting: the anastomosis is evident in the lowest of the encircled areas; however, repetitions or ghosts can be seen in the other encircled areas.

variation in the flow solution. The aim of this work is thus to take a representative example of an arterial geometry which commonly poses problems in image reconstruction, and to explore the above issues using this as a test case. Specifically, the issues addressed are sensitivity to smoothing, to idealization and to medical image thresholding.

The geometry studied in this work is an end-to-side anastomosis performed using the tunnelling technique. The anastomosis was below-knee and popliteal, the graft conduit was a long saphenous vein. We consider as a data set a single MR image stack acquired using a 2D time-of-flight scanning sequence with 0.25 mm in plane pixel spacing, 1.5 mm slice spacing and 1.5 mm slice thickness. For further information on the patient-specific data, see [9, 10, 20].

We consider two related arterial geometries, reconstructed using different constant threshold choices. We also consider the effects of surface smoothing and geometry idealization by fitting elliptical cross sections to a third geometry, reconstructed manually by an experienced user. The geometric variation is thus confined to the small-scale features brought about by these uncertainties, whilst the global features of the geometry are invariant.

The outline of the paper is as follows. Section 2 presents: the virtual model reconstruction from the MR image stack, segmentation criteria, which are based on a user-defined choice and variations on automatic procedures, and interpolation using an implicit function formulation to give a continuous surface. Section 3 discusses a skeletonization procedure that permits the characterization of the geometry of the bypass graft using the angles subtended by the best line fit to the skeleton branches, and their cross-sectional area variation. Different smoothing procedures are discussed in Section 4 based on three different requirements: firstly, smoothing the skeletons to obtain smoothly varying tangents; secondly, initial smoothing of the interpolated surface to reduce the artefacts in the reconstruction procedure; thirdly, subsequent smoothing of the surface to reduce topological detail. Section 5 describes an idealization of the geometry by fitting elliptical sections to the segmented contours of the image stack that will be used to compare topological details and sensitivity to the flow. Section 6 summarizes the different variations to the geometry and their effect on WSS. Finally, conclusions are given in Section 7.

DOI: 10.1002/fld

2. GEOMETRY RECONSTRUCTION AND IMAGE THRESHOLD

2.1. Image segmentation and effects on threshold

Initial processing of the images involves a *maximum intensity projection* of the image stack and selection of the region of interest (ROI). Subsequent processing is confined to the ROI, reducing the computing cost. The *contrast-to-noise ratio* (CNR) can be used to help quantify the goodness of the image quality and is used as an initial measure of the possible errors associated with the reconstruction of the virtual models. It is defined as

$$\mathrm{CNR} = \frac{S_{\mathrm{ROI}} - S_{\mathrm{ST}}}{\sigma_{\mathrm{NOISE}}} \tag{1}$$

where S_{ROI} and S_{ST} are the signal intensities (or mean square amplitudes) in the ROI and the surrounding tissue (ST), respectively, and σ_{NOISE} is the standard deviation of the signal intensities of the surrounding ROI background [21]. For the image stack used here $\mathrm{CNR} = 1.9$ which can be considered to be good, i.e. the noise level in the image is low. The grey-scale pixel intensity levels of the image stack in the ROI are then normalized to span the range $(0, 255)$.

Two thresholding techniques will be considered: constant threshold selection over the image stack and the region growing method.

Choosing a threshold of constant grey-scale level for an image is a simple yet effective method to delineate a feature. Assuming that there is a clean distinction between signal intensities internal and external to the conduit, the edge pixels defining the internal vessel boundary are identified by this threshold. This set of pixels provides the initial definition of the surface of the flow passage that we will reconstruct numerically to form a computer model.

The region growing method of segmentation used here works by gradually decreasing the choice of seed point grey-scale threshold until the point where the segmented lumen area suddenly increases.

Here three different contour stacks are obtained from the medical images by using different thresholding criteria. The first set of contours was produced based on an experienced user's choice of the threshold level that should be chosen for each medical image individually. This set of contours will be referred to as geometry G_U and will be discussed later. Two further geometries G_1 and G_2 were obtained by choosing constant threshold values of $T_1 = 50$ and $T_2 = 65$, respectively, in the normalized grey scale. The mean distance between the two reconstructed geometries G_1 and G_2 is less than 0.5 pixels which is within user uncertainty bounds for segmentation (see Figure 2). The values of T_1 and T_2 were guided by considering both a region growing method and constant threshold choices. The region growing method yielded a mean value of 55.7 on the grey scale. The constant threshold value over the stack which yields the smallest variation in geometry with respect to grey-scale threshold level choice was found to be 60.4. This latter approach was performed by segmenting the image stack for a range of thresholds and describing the smallest variation in geometry as the mean closest distance between the closed curves stack. A 3% variation in the approximate mean of these two values yielded T_1 and T_2 and represents a realistic range of deviations from the true geometry, being neither extreme nor unreasonable segmentation.

2.2. Surface interpolation using implicit functions

As part of the reconstruction procedure, we require to interpolate the stack of contours obtained from medical image segmentation to obtain a continuous surface. The proposed method for interpolating

DOI: 10.1002/fld

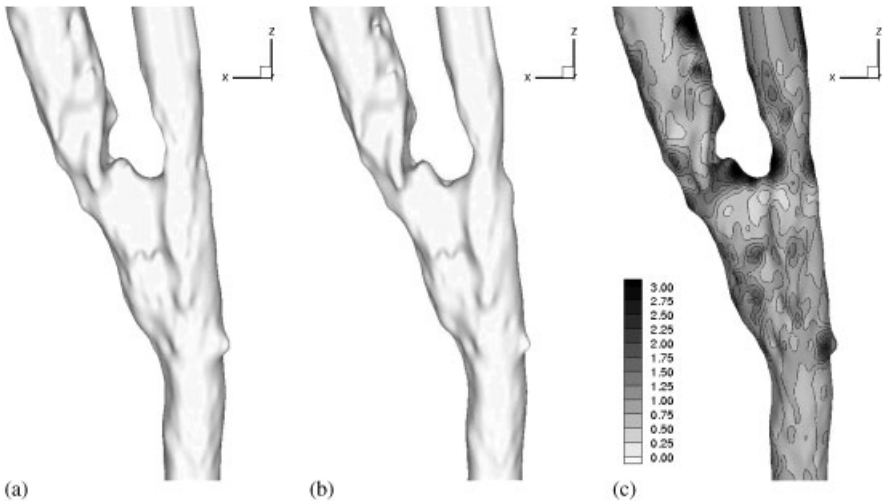

Figure 2. Geometries (a) G_1 and (b) G_2 obtained from segmenting the image stack with constant thresholds T_1 and T_2, respectively. (c) Distance map between the surfaces of G_1 and G_2 (scale corresponds to distance in pixels).

a surface through the contour stack is described in previous work [20, 22] and we only outline the procedure.

The geometry is defined as the zero-level iso-surface of an implicit function $f(x, y, z)$. This is done by setting $f(x, y, z) = 0$ on equally sampled points of the closed contour stack obtained from the medical images, known as *on-surface* constraints. A gradient is formed in the implicit function by introducing further constraints with negative values inside the curves at a constant close distance normal to the curve, known as *off-surface* constraints where $f(x, y, z) \neq 0$. A regular spacing of constraints reduces the computational cost to solve the system in Equation (3) [23]. Typically, a larger number of on-surface constraints are used to ensure an accurate representation of the surface.

Radial basis functions [24–26] are used to uniquely interpolate the constraints. If we consider a set of n constraints in $\mathbb{R}^3$ given by $\mathbf{x}_i = (x_i, y_i, z_i)$; $i = 1, \ldots, n$, where each constraint has a value of h_i such that $f(\mathbf{x}_i) = h_i$, then the implicit function can be expressed as

$$f(\mathbf{x}_i) = P(\mathbf{x}_i) + \sum_{j=1}^{n} \mathbf{c}_j \phi(\mathbf{x}_i - \mathbf{x}_j) \tag{2}$$

where $\phi(\mathbf{x}_i - \mathbf{x}_j)$ is the radial basis function and $\mathbf{c}_j$ is a set of coefficients. $P(\mathbf{x}_i)$ is a polynomial that accounts for the linear and constant portions of f and can be omitted for large n [27]. This can be expressed as a linear system of algebraic equations:

$$\mathbf{Ac} = \mathbf{h} \tag{3}$$

DOI: 10.1002/fld

where $\mathbf{A}_{ij} = \phi(\mathbf{x}_i - \mathbf{x}_j)$ is a non-singular $n \times n$ matrix. From [9, 10, 25] the choice of the radial basis function is

$$\phi(\mathbf{x}_i - \mathbf{x}_j) = |\mathbf{x}_i - \mathbf{x}_j|^3 \tag{4}$$

where $|\cdot|$ denotes the Euclidean norm.

The linear system is solved using the generalized minimal residual method. The number of constraints typically used in this work is of the order of 30 000. We introduce non-zero values on the diagonal of $\mathbf{A}$ to improve the computational time, which is equivalent to approximating the implicit function to pass close to the constraints to produce a smooth interpolation in the presence of noise [28]. Typical values for the diagonal terms of $\mathbf{A}$ are of the order of 10^{-3} pixels.

The extraction of the zero-level iso-surface is accomplished by using the marching cubes method to obtain an initial triangulation. The marching cubes method samples the value of the implicit function at the vertices of a lattice of cubes containing the geometry. Linear interpolation on the cube sides allows identification of the surface and hence meshing. The poligonizer algorithm used is implemented in [29] and it is based on the work of Bloomenthal [30].

3. TOPOLOGY CHARACTERIZATION *VIA* SKELETONIZATION

In order to assess differences in reconstructed geometries and their effect on the flow, we require a means to characterize the geometry. For example, such parameters include: cross-sectional area variation, average diameter of branches, approximate anastomosis diameter and angles between skeleton branches. Medial lines are used in this work as a means of representing the topology in a compact and quantifiable way that allows these measures to be calculated accurately.

The notion of thinning or skeletonization to yield a medial line or skeleton was introduced by Blum [31]. The skeleton is the supporting structure to the geometry which is the locus of the centres of the maximally inscribed spheres inside the object. The skeleton may be obtained from a binary 3D object by the use of a fast 6-subiteration algorithm [32].

The method used is one of a number of algorithms based on a binary representation of the volume; other approaches are discussed in [33]. The 3D binary digital picture of the object is defined in the 3D digital space $\mathbb{Z}^3$ such that each voxel is adjacent to 26 voxels. Each voxel inside the object is assigned a value of 1 while all the remaining voxels are assigned a value of 0. The thinning of the voxels to obtain the skeleton is iterative and removes the voxels with value 1 by applying a set of masks as presented in [32]. For the geometries used, the number of iterations was below 20. Various stages of the iterative process are illustrated in Figure 3.

The skeleton points obtained can be clustered into paths by identifying individual points and their adjacent neighbours. The points can be identified as belonging to one of three categories: a *line-end point* that has exactly one point adjacent to it, a *line point* with exactly two points adjacent to it and a *cross-point* that has more than two points adjacent to it. Using this classification it is possible, by simply exhaustively marching in all possible directions and ensuring no repetition of paths, to obtain paths starting at a line-end point or a cross-point and ending at a line-end point or a cross-point connected by line points.

An anastomosis consists essentially of three conduits and its skeleton is formed by three branches meeting at one point. Small spurious branches may appear in the skeletonization process. These can be due to local features on the surface of the topology as well as the discretization of the space in $\mathbb{R}^3$ to yield the digital space in $\mathbb{Z}^3$. Automatic clustering of the points into paths allows

DOI: 10.1002/fld

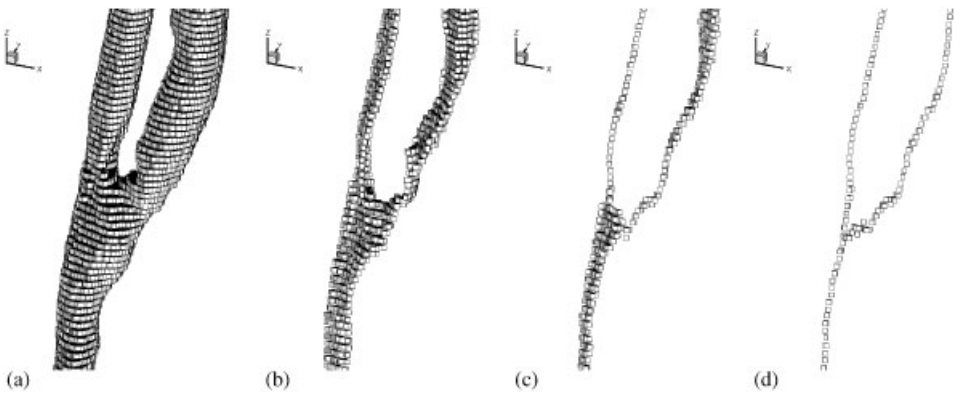

Figure 3. Skeletonization of the peripheral bypass graft in $\mathbb{Z}^3$: (a) initial binary image; (b) after 5 iterations; (c) after 10 iterations; and (d) after 17 iterations when the skeletonization process has terminated.

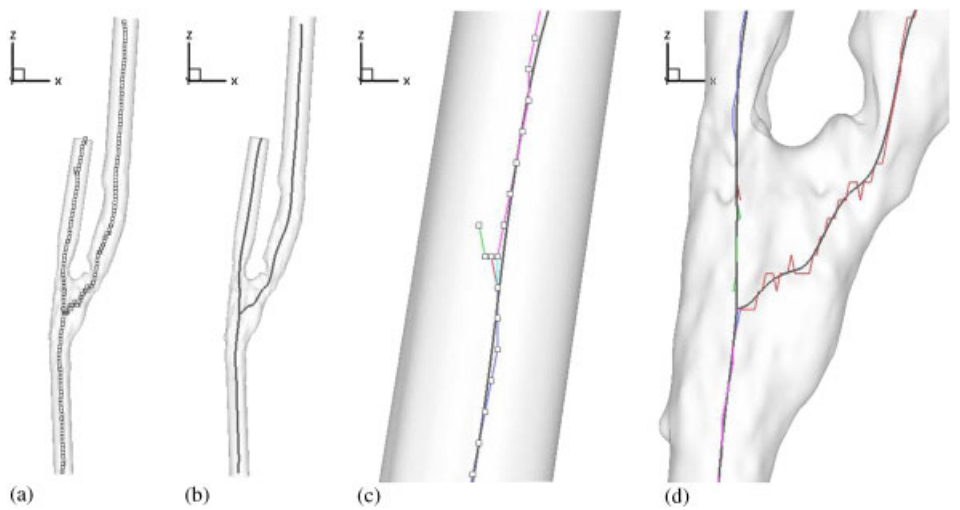

Figure 4. Skeleton of the geometry: (a) cloud of disorganized points obtained from the thinning process; (b) final smooth skeleton; detail of pixelated skeleton showing spurious branches and final smoothed and pruned skeleton for (c) proximal vessel and (d) anastomosis region.

spurious paths to be identified and removed, which is known as pruning. In the graft geometry, pruning leaves the three main skeletons corresponding to the distal, proximal and bypass graft vessels (Figure 4).

The representation of the skeleton obtained from this procedure is jagged since it is derived from the thinning of voxels and hence reflects the discrete nature of the image stack. Smoothing of the skeletons is therefore required and can be performed by the algorithms described in Section 4, constraining the line-end points and the cross-point not to move.

DOI: 10.1002/fld

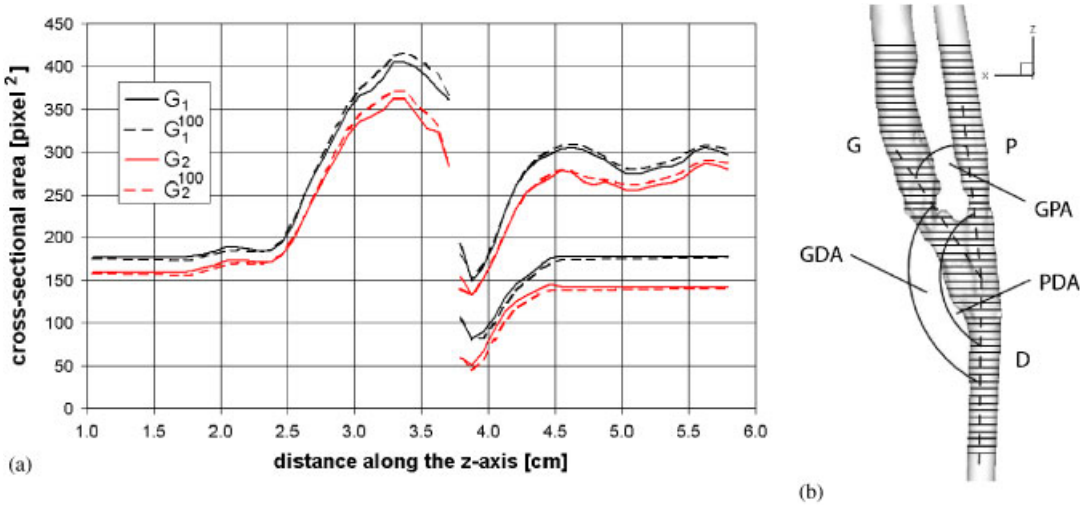

Figure 5. (a) Cross-sectional area for geometries G_1, G_2 (created using different constant thresholds T_1 and T_2 on the image stack) and their smoothed geometries G_1^{100} and G_2^{100}. The location of the sections are indicated in (b), taken at equal intervals and perpendicular to the z-axis. The graft (G), proximal (P) and distal (D) vessels are indicated in (b).

Having obtained the smoothed skeletons belonging to the three conduits, we can now extract measures to characterize the geometry. Once the average cross-sectional areas of each branch are calculated using the skeleton points and tangents to define the cutting planes, the average diameter of the branches is given by

$$L_1 = 2\sqrt{\frac{A_G + A_D + A_P}{3\pi}} \tag{5}$$

where A_G, A_D and A_P are the average cross-sectional areas of the graft, distal and proximal branches, respectively, as illustrated in Figure 5(b). The average is performed over the entire branch length available in the scan and we find $A_P = 9.99$, $A_D = 12.1$ and $A_G = 16.0\,\text{mm}^2$ for the user-segmented geometry. The second reference length L_2 is defined as the distance between the bifurcating point of the skeleton branches and the apex of the anastomosis, the location where the graft and the proximal branches separate. The apex location is found by calculating the shortest distance from the centroid of the distal branch exit over the surface of the graft [34]. The apex is the location where the contours of equal distance from the exit last join before dividing into the graft and proximal branches. The geometry reference lengths are calculated here as $L_1 = 4.0\,\text{mm}$ and $L_2/L_1 = 1.3$ ($L_2 = 5.2\,\text{mm}$).

The characteristic angles of the bifurcation of the anastomosis are defined as the minimum angles between the best-fit lines of the branches resulting in three angles: GPA $= 26°$, GDA $= 150°$ and PDA $= 172°$ which stand for graft–proximal angle, graft–distal angle and proximal–distal angle, respectively. The planarity of the graft is characterized by the angle, θ, between the graft and the plane formed by the distal and proximal conduits. For this geometry $\theta = 1°$. It is important to note that these angles do not change significantly with the geometries created.

DOI: 10.1002/fld

4. SURFACE SMOOTHING OF GEOMETRY

To understand the significance of small-scale geometrical features on the flow, we have applied several degrees of smoothing to the user-defined segmentation reconstructed geometry. The small-scale features are typically of the order of 1 pixel and are present in the regions of high curvature.

We have used three smoothing schemes: Laplacian, bi-Laplacian and projected mean curvature methods to deal with three different aspects. Firstly, the Laplacian method was used in the skeletonization procedure to obtain a smoothly varying tangent. Secondly, the bi-Laplacian is used on the reconstructed mesh to regularize the mesh and remove artefacts in the RBF interpolation and marching cubes procedures. Thirdly, the projected mean curvature method has been used for subsequent smoothing, after the bi-Laplacian smoothing, to generate different idealized geometries, as discussed in Section 6.

The smoothing of the surface is performed as follows. Let us consider a regular triangular mesh consisting of N vertices $\mathbf{v}_i=(x_i, y_i, z_i)$; $i=1,\ldots,N$. The neighbouring vertices to each vertex $\mathbf{v}_i$ in the triangulation are denoted by $\mathbf{v}_j$; $j=1,\ldots,m_i$, where m_i is the number of neighbours. The discrete Laplacian at the vertex $\mathbf{v}_i$ is calculated as

$$\mathbf{L}_i=\sum_{j=1}^{m_i} w_{ij}(\mathbf{v}_j-\mathbf{v}_i) \tag{6}$$

where the weights w_{ij} can be given by various functions [35] with the constraint that $\sum_{j=1}^{m_i} w_{ij}=1$. In this work we use $w_{ij}=1/m_i$. The Laplacian can then be interpreted as the vector moving the node in question to the barycentre of the neighbour vertices.

The smoothing algorithm is iterative: the mesh nodes $\mathbf{v}_i^n$, where n denotes the iteration number, are moved simultaneously to a new position

$$\mathbf{v}_i^{n+1}=\mathbf{v}_i^n+\lambda\mathbf{L}_i^n, \quad 0\leqslant\lambda\leqslant 1 \tag{7}$$

This form of smoothing, known as Laplacian smoothing, produces large amounts of shrinkage of the surface. To overcome this, an inflation step is introduced as part of the smoothing:

$$\begin{aligned}\mathbf{v}_i^{n+1/2}&=\mathbf{v}_i^n+\lambda\mathbf{L}_i^n\\ \mathbf{v}_i^{n+1}&=\mathbf{v}_i^{n+1/2}+\mu\mathbf{L}_i^{n+1/2}\end{aligned} \tag{8}$$

where the Laplacian is recalculated at each step. If $\mu=-\lambda$ this is known as bi-Laplacian smoothing.

An alternative smoothing method is obtained by considering the curvature κ_i in the normal direction $\mathbf{n}_i$ at vertex $\mathbf{v}_i$, calculated using the formula proposed in [36] and given by

$$-\boldsymbol{\kappa}_i\mathbf{n}_i=\frac{1}{4A_i}\sum_{j=1}^{m_i}(\cot\alpha_j+\cot\beta_j)(\mathbf{v}_j-\mathbf{v}_i) \tag{9}$$

where A_i is the area of the triangles surrounding node $\mathbf{v}_i$ and α_j and β_j are the angles opposite to side ij in the triangles sharing this side. The curvature normal can be normalized using the radius of an equivalent circle of area A_i and is defined as $\mathbf{K}_i=-\boldsymbol{\kappa}_i\mathbf{n}_i\sqrt{A_i\pi}$. If $\mathbf{K}_i$ is used instead of $\mathbf{L}_i$ in Equation (7) it tends to cluster the points, distorting the mesh. Mesh regularization is obtained

DOI: 10.1002/fld

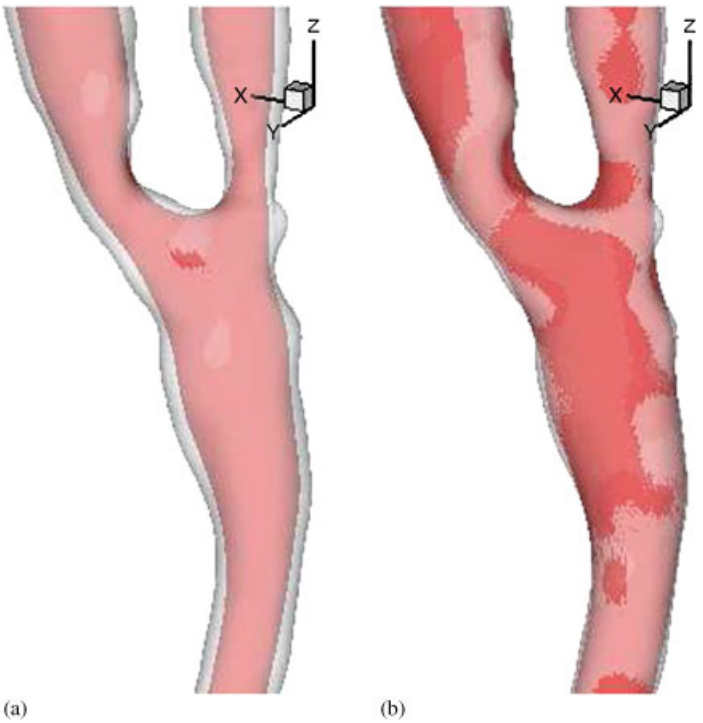

Figure 6. Geometry G_1, seen as white, has been smoothed using 100 iterations of the projected mean curvature flow method and yields the red surface in (a). Subsequent inflation by movement along the surface normal by the mean closest distance between the surfaces yields geometry G_U^{100} coloured in dark grey in (b).

by projecting the normalized curvature normal onto the Laplacian barycentre vector and Equation (7) now becomes

$$\mathbf{v}_i^{n+1} = \mathbf{v}_i^n + \lambda(\mathbf{L}_i^n \cdot \mathbf{K}_i^n)\frac{\mathbf{L}_i^n}{|\mathbf{L}_i^n|} \tag{10}$$

yielding the so-called projected mean curvature flow smoothing [37].

The above schemes act as low-pass filters to curvature with no compensation of the removed higher frequencies. The result is that the surface will shrink with increased number of smoothing iterations. To overcome this the surfaces are re-inflated after the smoothing has been terminated. The inflation is performed iteratively by moving each vertex by the average closest distance between the geometries along the local normal, and is found to be effective even with severe shrinking as can be seen in Figure 6. The inflation performed in this way does not guarantee that the volume is maintained but does minimize the distance between the surfaces. Maintaining the fit of the smoothed surfaces to the original surface is of importance here in order to avoid large anatomical changes and maintain the cross-sectional area.

DOI: 10.1002/fld

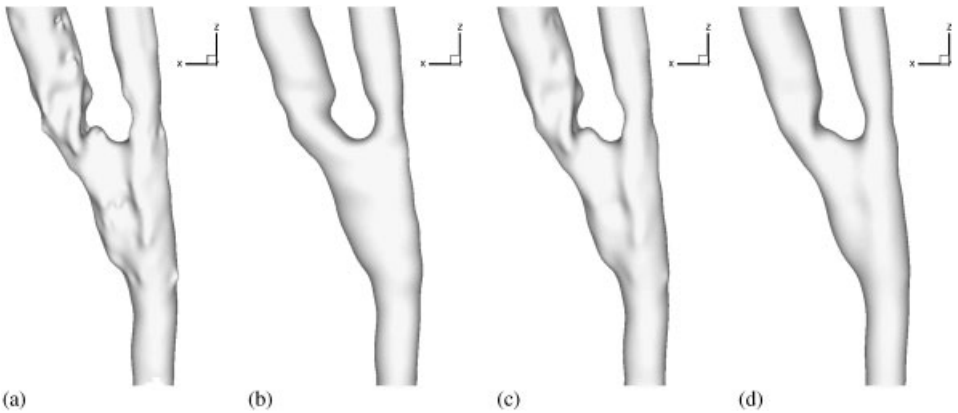

Figure 7. Comparison of geometries defined by: (a) user segmentation (G_U) and (b) geometry idealized by elliptical fitting (G_E). Effect of smoothing on geometry G_U is shown in (c) for 20 iterations of the projected mean curvature flow to obtain G_U^{20} and (d) 100 iterations to yield G_U^{100}.

All geometries were obtained directly from the reconstructed geometry by using 50 bi-Laplacian iterations with $\lambda = -\mu = 0.6$. The mean closest distance due to this smoothing is of the order of 0.01 pixels for all the geometries. This does not alter the flow solution significantly.

Further smoothing iterations are performed on these geometries using the projected mean curvature algorithm with $\lambda = 0.1$ followed by a re-inflation once the smoothing is terminated.

Figure 7 shows a set of successively smoothed geometries, progressing from what could be described as slight retouches to such a high degree of smoothing so as to cause significant differences from the original geometry, leading to a form of idealized geometry. For comparison, an idealized geometry obtained by ellipse cross-section fitting, which will be discussed in Section 5, is also shown in this figure.

5. ELLIPTICAL SECTION FITTING

An alternative approach to reconstructing the geometry is to fit elliptical sections to the curves segmented from the MR images. This reduces the complexity of the anastomosis geometry. Apart from providing a means to idealize the geometry, the technique of reconstruction using elliptical sections is also used when more limited *in vivo* imaging data are available, for example, in multi-planar angiography. The result is a stack of ellipses that best represents the segmented contour stack obtained from the medical images. An implicit function is then interpolated between the slices to reconstruct the surface.

The ellipses are chosen individually for each contour so that they lie in the same plane, have the same cross-sectional area and the centre of the ellipse coincides with the centre of the closed contour section. This is performed using the proper orthogonal decomposition method. Each closed contour is re-sampled to have equally spaced points $\mathbf{p}'_i = [x'_i, y'_i, z'_i]^{\mathrm{T}}$ for $i = 1, \ldots, n$. These points

DOI: 10.1002/fld

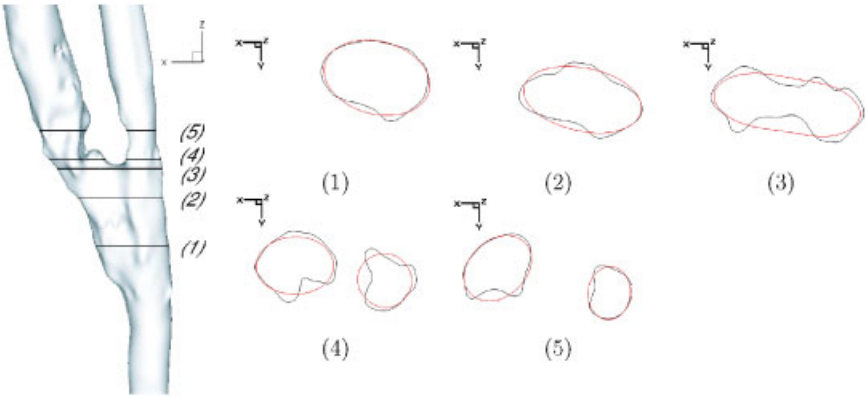

Figure 8. Location of sections taken to compare geometries G_U and G_E. The slices are ordered from (1) to (5) according to increasing z coordinates.

are mean subtracted to remove the bias such that $\mathbf{p}_i = \mathbf{p}'_i - (1/n)\sum_{j=1}^{n} \mathbf{p}'_j$ and then assembled to form a $3 \times n$ matrix $\mathbf{P}$. The covariance matrix is given by

$$\mathbf{C} = \frac{(\mathbf{P}\mathbf{P}^{\mathrm{T}})}{n} \tag{11}$$

The unit eigenvector corresponding to the largest eigenvalue of $\mathbf{C}$ is the major axis of the ellipse, the unit eigenvector corresponding to the second largest eigenvalue is the minor axis of the ellipse while the last unit eigenvector is the normal to the plane containing the ellipse and its eigenvalue has zero magnitude.

A few slices have been taken from the ellipse fit geometry and compared with that of its reference geometry in Figure 8, which shows the reduction in complexity of the cross sections whilst preserving their area.

6. ANALYSIS OF THE EFFECTS OF SHAPE VARIATION ON FLOW

6.1. Flow conditions and methodology

We are particularly interested in the flow distribution in the regions of the heel, toe and floor of the anastomosis, highlighted in Figure 10, since these are regions of low WSS and preferential sites for the development of intimal hyperplasia [38]. Intimal hyperplasia is manifested by an abnormal change in the cellular structure of the vascular wall; an over-proliferation of the smooth muscle cells occurs and the interior passageway or lumen available to the flow is progressively reduced. Eventually, the anastomosis becomes no longer patent and the graft fails.

All the results presented are for the anastomosis which is taken to be the region within a distance L_2 from the beginning of each branch.

The mean velocity was measured by Doppler ultrasound. Blood is assumed to be an incompressible Newtonian fluid. The Reynolds number based on the bypass conduit inflow diameter was found to be $Re = 135$, low enough for the flow to be considered laminar, with a 40% proximal and 60% distal outflow split. The Womersley number is $\alpha \approx 3$ which justifies assuming a steady flow.

DOI: 10.1002/fld

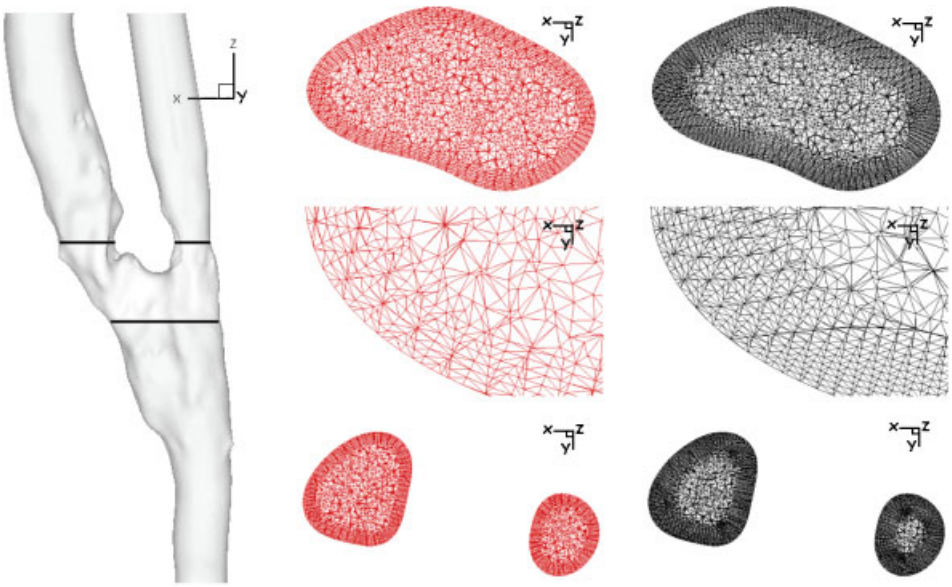

Figure 9. Location and sections of the mesh volume used to test for mesh convergence. The meshes consist of approximately 1.7 and 4.3 million cells.

The inflow boundary condition is taken to be a Poiseuille flow velocity profile and the simulations are performed using Fluent 6.0.12 second-order, segregated, SIMPLE method flow solver [39].

A volume mesh with eight prismatic elements across the boundary layer is generated using TGrid [40]. The height of the prismatic elements nearest to the wall is 5.5×10^{-5} m corresponding to 2.3% of the bypass inflow radius. The unstructured mesh contains approximately 1.7 million cells. The spatial resolution of this mesh was considered to be fine enough for mesh convergence since a finer mesh with 4.3 million cells and 12 prismatic boundary layer elements (with initial element height of 4.3×10^{-5} m corresponding to a 1.8% of the bypass inflow radius), see Figure 9, produced a relative difference in WSS smaller than 0.01%.

To summarize, a set of geometries is formed from the same medical image stack to represent plausible uncertainty and variability in the segmentation and reconstruction schemes. The mean segmentation variability in the reconstructed geometries is below 0.5 pixels. Two initial geometries, referred to as G_1 and G_2, are obtained by reconstructing the medical image stack using constant threshold values of T_1 and T_2, respectively. A further geometry G_U is obtained from a user-defined segmentation of the stack and its idealization by fitting elliptical section is called G_E. Only G_U is subjected to a range of smoothing intensities using the projected mean curvature method to observe the trend from small topological variations, corresponding to few smoothing iterations, to larger changes which simplify the geometry greatly when the number of iterations increases. The number of smoothing iterations performed are 10, 20, 60, 80 and 100. The nomenclature for the smoothed geometries is to place the number of smoothing iterations as a superscript so that, for example, G_U^{20} denotes geometry G_U, the user-defined segmentation, after 20 iterations of smoothing. All these geometries were analysed but, for simplicity, only the images of G_U, G_U^{20}, G_U^{100}, G_E, G_1 and G_2 are shown as indicative examples.

DOI: 10.1002/fld

In comparing the flow in the different geometries, we examine the geometric variation in terms of curvature change and the closest distance between the different model surfaces. The value of the closest distances are normalized by the pixel size and the WSS are normalized by the value of WSS at the graft inlet. We utilize as a mapping a point-to-surface correspondence based on the closest distance from the reference surface to the target surface, which defines the corresponding closest location. A measure of the reduction of the small-scale features is the reduction in mean curvature of the surface, calculated using Equation (9), with respect to the reference geometry. Geometric deviations between surfaces are characterized directly by the closest distance map. By mapping the WSS and curvature (hence surface properties) of an interrogation geometry onto the reference geometry and calculating the distance between the surfaces, a measure of the change of geometry and its effect on the flow can be obtained.

6.2. Effects of surface smoothing on the flow

Here we consider the effect of smoothing on geometry G_U which is obtained from the user-defined segmentation. The geometries include G_U^{20} and G_U^{100} which are obtained from smoothing using 20 and 100 iterations, respectively, and G_E which is obtained by fitting elliptical cross sections.

We will first examine the results of progressive smoothing applied to geometry G_U, from 'mild' to 'severe' smoothing.

Most of the reduction in mean curvature occurs in the first few iterations. Changes in the geometry in the early smoothing iterations correspond to reduction of small-scale features while the later iterations correspond to the gross removal of features and hence a noticeable simplification in the detail of the surface geometry. Small-scale alterations to the geometry tend to be in the locations of high curvature only and the effect is typically not confined to where the movement has occurred but propagates downstream and hence there is less direct correlation. When a large number of iterations is performed, some of the lower curvature regions are also affected leading to an idealization and topological change on a larger scale. It is evident that the changes in G_U, due to mild smoothing to obtain G_U^{20}, are more closely linked to the small-scale features. It is only in applying severe smoothing to obtain G_U^{100} that the effects of idealization start to become readily noticeable. This can be observed in Figure 7.

Sensitive indicators of the change in flow structure with geometry variations are the distribution of WSS and corresponding surface shear lines. The surface shear lines are aligned with the tangential component of the viscous traction exerted by the flow on the wall. They indicate the limit in the direction of the flow velocity vector as the wall is approached, and are useful in highlighting zones of attachment and separation.

Comparing the surface shear lines for different degrees of smoothing, the results shown in Figure 10 demonstrate that the reduction in small-scale geometric irregularity results in a more coherent pattern of shear lines. Likewise, the contour plot of streamwise velocity at a cross section through the anastomosis shows how the velocity distribution is effectively simplified. Clearly, G_U^{100} and G_E show similar features which can be thought of as alternative topological simplifications due to smoothing in one case and elliptical fitting in the other.

In terms of detailed haemodynamics, the regions of separation at the toe of the anastomosis and the stagnation point due to the impact of the jet coming from the graft at the floor are clearly evident. A small separation region at the heel in G_U and G_U^{20} can also be observed, but this feature is removed in the case of high smoothing, G_U^{100} and in the idealized geometry G_E. The location of the stagnation point on the floor of the anastomosis is seen not to change significantly

DOI: 10.1002/fld

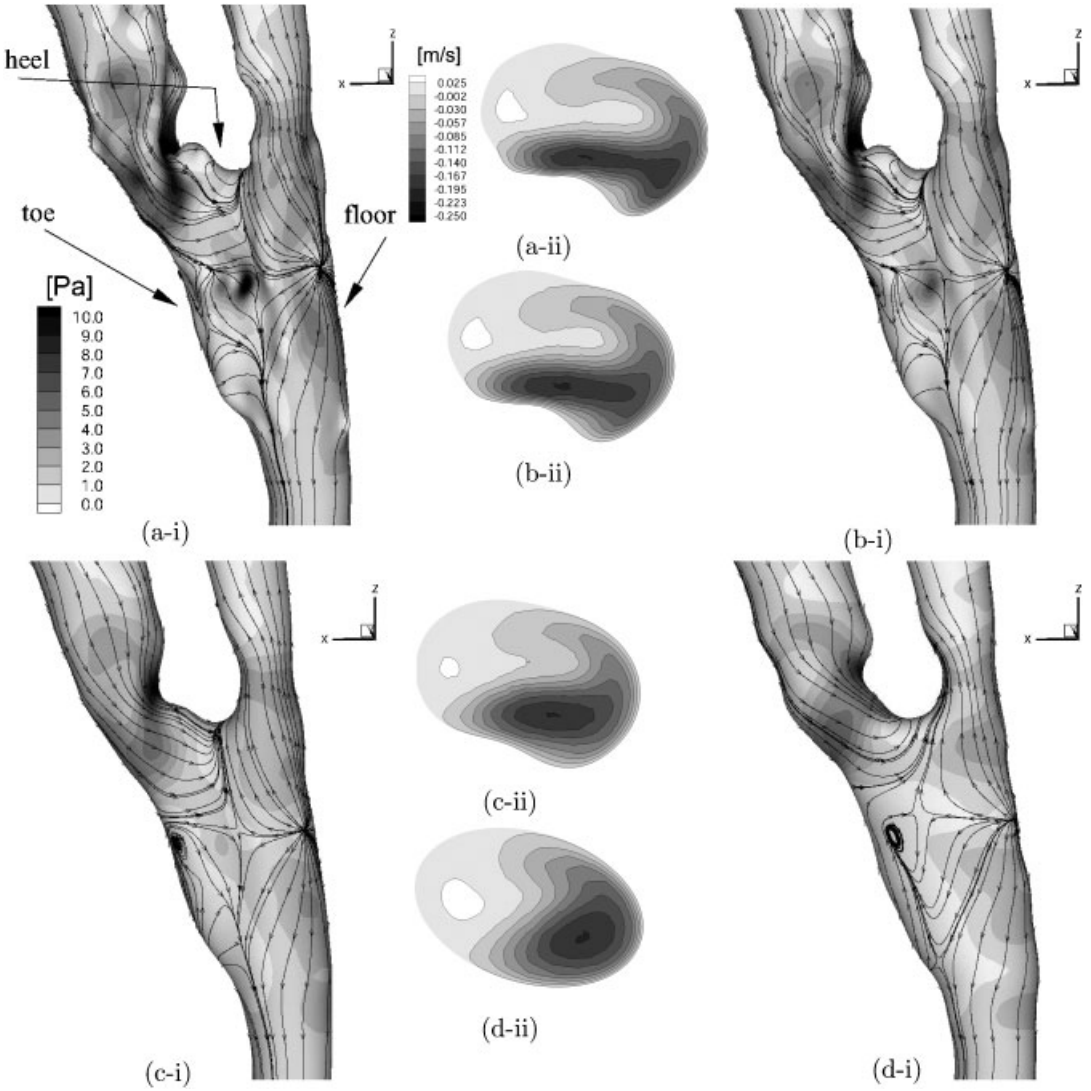

Figure 10. Influence of geometric variations on wall shear stress magnitude (Pa), surface shear lines and the z-component velocity (m/s): (a) G_U, (b) G_U^{20}, (c) G_U^{100}, and (d) G_E. The cross section is section (1) in Figure 8.

for any of the geometries: with respect to G_U the change in location is approximately 0.5 pixels for G_U^{20}, 1.7 pixels for G_U^{100} and 2.1 pixels for G_E. This indicates that the stenosis in the graft is a dominating feature in directing the graft flow into the anastomosis. The separation region at the toe does not appear to change significantly in spatial extent, although the strength of the flow reversal appears to increase slightly (from the spacing and orientation of the shear lines). There is also an increasingly noticeable swirling motion in this region as the geometry is progressively

DOI: 10.1002/fld

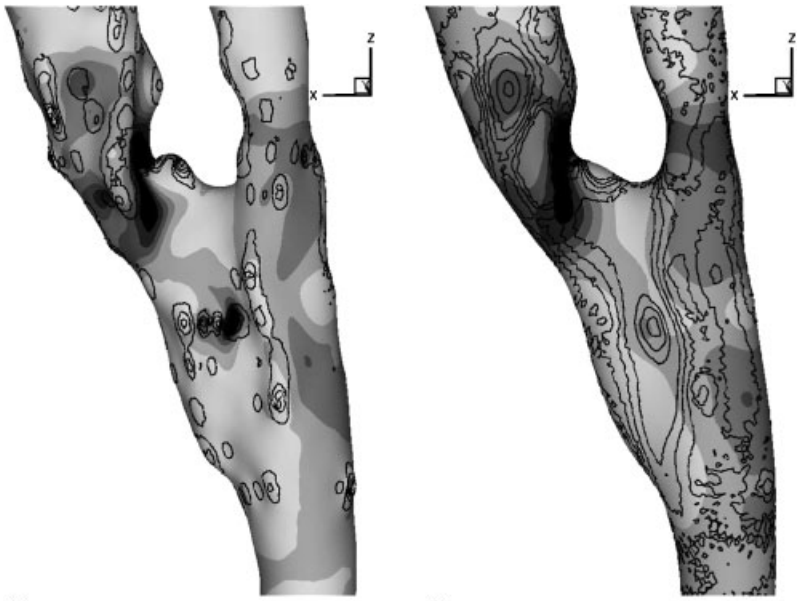

Figure 11. Geometries (a) G_U, (b) G_U^{100} with wall shear stress shading, black lines represent curvature iso-contours. The scale has been normalised to have the same range, from minimum to maximum, for all parameters. Note that (i) correspondence between extrema of curvature and WSS is noticeable only before the stenosis and (ii) smoothing the geometry produces a more gradual change in the WSS, but downstream of the stenosis the extrema in curvature and WSS are poorly correlated.

smoothed or simplified, where the fluid leaves the surface. However, this has been observed to be of small intensity using the vortex structure identification method described in [41].

The correspondence between the WSS and the small-scale features of the geometry is observed using the curvature as an indicator, as seen in Figure 11. It has been found that for geometry G_U there are smaller and more localized pockets of higher curvature and also of WSS while for the smoothed case G_U^{100} the changes in curvature and WSS are more gradual. The impact of smoothing the geometry is noticeable on the WSS. However, the correspondence of the regions of curvature and WSS is not evident after the stenosis but more so in the graft before the stenosis, especially for G_U. Upstream of the stenosis the flow is attached and there is strong correspondence between the curvature and WSS, whereas the flow recirculation in the anastomosis downstream of the stenosis destroys this correspondence. Therefore, it is evident that the stenosis dictates the gross flow behaviour and the correspondence between the WSS and the curvature is not localized after the stenosis.

Table I and Figure 12 show that the changes in average normalized WSS and average normalized closest distance are progressively larger with progressively higher degrees of smoothing, but their correspondence is not as linear as might initially appear in Table II. The surface movement due to the smoothing occurs initially at the regions of higher curvature. However, further iterations alter the larger scale features and hence the overall surface movement is no longer confined to the locations of higher curvature.

DOI: 10.1002/fld

Table I. Variations, measured as area-weighted averages over the geometry surfaces and performed only in the anastomosis region of interest given by considering only L_2 of the branch lengths.

Geometry	Curvature change (%)	Normalized WSS difference (%)	Closest distance (% pixel)	Area change under 1.0 Pa (%)
G_U–G_U^{20}	8.4	11.8	0.8	1.3
G_U–G_U^{100}	12.9	23.7	3.4	3.0
G_U–G_E	14.3	48.3	4.6	4.5
G_1–G_2	3.6	55.6	49.2	9.8

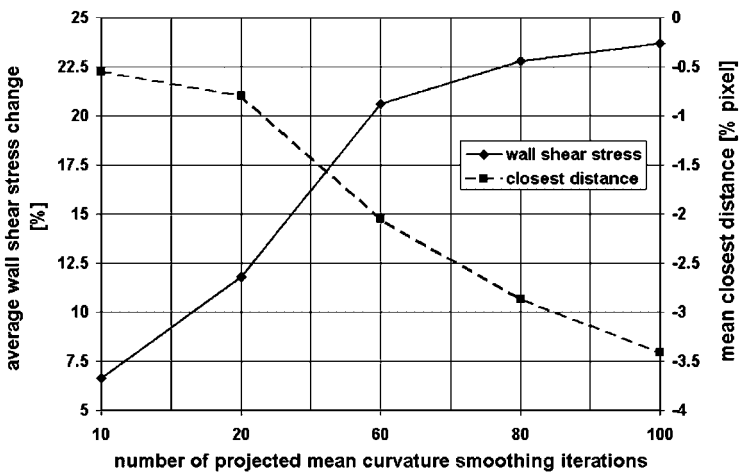

Figure 12. Average normalized wall shear stress difference (%) and average closest distance (% pixel) for the different intensities of smoothing due to increased number of iterations performed.

The maximum and minimum variation of WSS along the conduits decrease with increased smoothing, as seen in Figures 13 and 14, indicating that the flow is more uniform. The small-scale features that introduce higher curvature also increase the peaks of the WSS whilst reducing the average value of WSS. The maximum and minimum WSS variations for G_E are similar in magnitude to those for G_U^{100}.

The Pearson correlation coefficient r is a simple statistical tool which gives a measure of the tendency of the variables to increase or decrease together. For two variables x and y, corresponding to the normalized WSS change and the normalized closest distance between the two surfaces, respectively, evaluating the variables at n surface points yielding n data points x_i and y_i; $i = 1, \ldots, n$. The Pearson coefficient is then defined as

$$r = \frac{(\sum_{i=1}^{n}(x_i - \overline{x})(y_i - \overline{y}))^2}{\sum_{i=1}^{n}(x_i - \overline{x})^2 \sum_{i=1}^{n}(y_i - \overline{y})^2} = \frac{\mathrm{cov}(x, y)}{\sigma_x \sigma_y} \tag{12}$$

where $\overline{x}$ and $\overline{y}$ denote the mean values, σ_x and σ_y denote the standard deviations, and $\mathrm{cov}(x, y)$ denotes the covariance. The value of r is such that $|r| < 1$. The results of the correlation are given in Table II and variables are considered to be strongly correlated if $|r|$ is close to 1. The results of

DOI: 10.1002/fld

Table II. Comparison of geometry and WSS: comparing the closest distance moved (y) with the WSS change (x) for corresponding points by using the Pearson correlation coefficient r and fitting a least-squares line of best fit through data such that $y=a+bx$.

Geometry	r	a	b
G_U–G_U^{20}	0.44	0.02	0.13
G_U–G_U^{100}	0.44	0.08	0.20
G_U–G_E	0.38	0.04	0.18
G_1–G_2	0.34	0.43	0.11

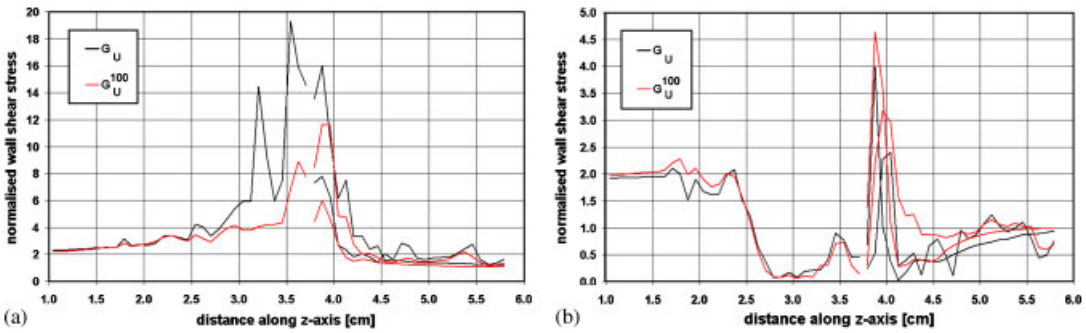

Figure 13. (a) Maximum and (b) minimum wall shear stress for geometries G_U and G_U^{100} in the location of the slices seen in Figure 5. The graft, proximal and distal conduits are divided at $z=3.5$ so that the smaller WSS values with large values of z are in the proximal branch.

the progressively more intensive smoothing cases, ranging from 10 iterations to 100 iterations in the smoothing, show the correlation to increase from $r=0.42$ when comparing G_U with G_U^{10} to $r=0.44$ when comparing G_U with G_U^{100}. Hence, there is not a significant change with smoothing. For these values of r the correlation is considered to be moderate.

As expected, the correlation of the distance moved with the WSS difference is not very large since an upstream change will have a downstream effect on the flow. The correlation coefficient appears to be smaller in the less smoothed cases also because the data are clustered in a small region due to small changes in both the WSS and distance; hence, not obtaining a large spread which would allow for a better correlation. A better correlation for the idealization by smoothing than for the ellipse fitting is noticeable.

6.3. Effects of threshold uncertainty in segmentation on the flow

We now consider geometries G_1 and G_2 created by constant threshold segmentation. When comparing G_1 with G_2 we must remember that the mass flow in each case is different since the Reynolds number has been maintained instead of the flow rate. Since we apply fully developed Poiseuille velocity profile at inflow and the diameters of the graft inflow are 4.83 and 4.70 mm for G_1 and G_2, respectively, we find that the WSS at inlet are 0.727 and 0.765 Pa, respectively, which would imply an increase of the straight pipe WSS by 5.2%. On comparing the WSS patterns

DOI: 10.1002/fld

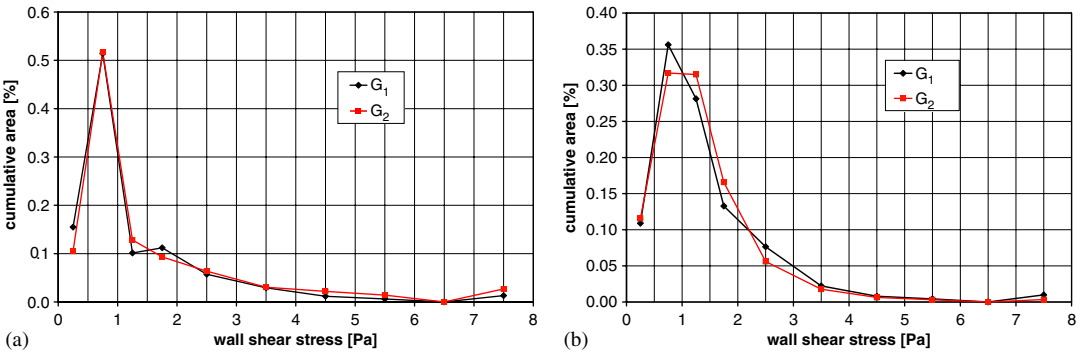

Figure 14. Cumulative area distribution for the wall shear stress. The effect of the different thresholding, importantly, is seen to have decreased the region of WSS < 0.5 Pa between geometries G_1 and G_2. Smoothing the geometry G_U tends to reduce the peaks of WSS as seen in Figure 13 while we see here and from Table I that the mean WSS increases.

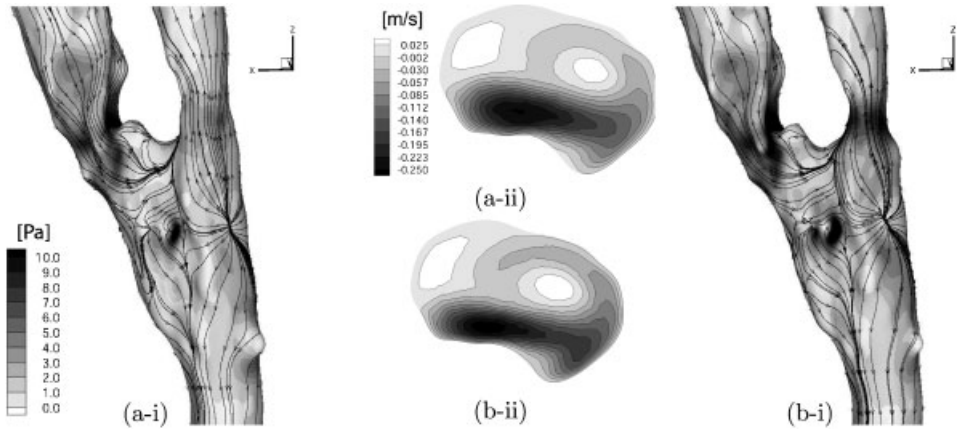

Figure 15. Wall shear stress magnitude (Pa), surface shear lines and the z-component velocity (m/s) section for geometries (a) G_1 and (b) G_2. The section location is the same as section (1) in Figure 8.

therefore, we need to keep this offset in mind. However, from observing the average positive WSS difference in Table I we see that the effects are highly non-uniform and there is a 55.6% change. This indicates that the flow does not behave linearly with respect to the cross-sectional area change and hence we cannot expect that the results for G_1 and G_2 are directly scalable. Furthermore, from the Pearson coefficient we note that the correlation in WSS change and closest distance between G_1 and G_2 is weak even though the average closest distance is under 0.5 pixels.

As summarized in Table I, the change in area with WSS < 1 Pa can be as high as 10%. More emphatically, as indicated by Figure 14, the region with WSS < 0.5 Pa varies by nearly 50% between the different reconstructed geometries. It should be noted that for this patient over 50% of the bypass geometry had a WSS < 1 Pa and in fact postoperative re-stenosis occurred resulting in re-operation to insert a jump graft, which also failed.

DOI: 10.1002/fld

Observing once again the surface shear lines for the WSS in Figure 15, we note that the general flow patterns to be very similar once again with no noticeable change in the stagnation point on the floor of the anastomosis (approximately 1.5 pixels) and the separation regions at the toe and heel of the anastomosis.

Unlike the results in Figure 10, a further significant region of positive z-component velocity is seen and corresponds to the flow going to the proximal vessel. This is of interest since the user-defined thresholds lie within the range of T_1 and T_2 for the anastomosis and therefore G_U would be expected to show flow characteristics ranging from those seen for G_1 and G_2.

7. CONCLUSIONS

These results represent a preliminary investigation of the impact of uncertainties in medical imaging reconstruction on the flow solution. Choosing as a test case the modelling of flow in a patient-specific peripheral bypass graft anastomosis, we have determined the likely range of uncertainty in the geometric boundary definition. Methods to assess the quantitative effect of such variations on the computed haemodynamics have been presented. The information derived and procedures described should be of benefit for further studies to incorporate uncertainty in evaluating the haemodynamics of different patient-specific geometries.

We found that, on average, artefacts in the MR image stack, processed by different segmentation and reconstruction methods to obtain the virtual model, yield small variations in the geometry (of the order of 0.5 pixels), but local changes can amount to several pixels as can be seen in Figure 2(c). Such changes were observed to occur in the vicinity of stenoses, which are regions of high sensitivity. As a consequence, the WSS distribution showed significant variations.

The mean point-wise change in the WSS resulting from different segmentations obtained with constant thresholds was found to be 55.6% (Table I), while the expected change due to the increased mass flow would only be 5.2%, based on the inflow WSS. Furthermore, it was demonstrated that the closest distance between corresponding points on different model surfaces cannot be correlated directly with the local WSS changes. As shown in Table II, the closest point correlation of WSS difference is $r=0.44$ whether small (20 iterations) or significant (100 iterations) smoothing is applied while $r<0.38$ for different constant threshold choices.

The work clearly indicates that the mean distance cannot be used exclusively as an indicative parameter in assessing the confidence bounds to the reconstruction process. However, it can, for now, be used together with the nominal solution to indicate the degree of sensitivity associated with the reconstruction process. This is unsurprising, given that changes to a stenosis, for example, will have significant effects downstream, but it nevertheless highlights the non-local correspondence between boundary displacement and flow consequence.

The results indicate that mild smoothing results in the simplification of small topological features, producing a more coherent pattern of shear lines (in which small irregularities are removed). By contrast, severe smoothing leads to geometrical changes which are dispersed over to the large scales tending towards geometrical idealization with correspondingly large alterations in WSS. These flow features are similar to those obtained fitting elliptical sections.

Overall, this work has shown the need to consider the effect of parameter uncertainty in attempting to derive quantitative measures from patient-specific studies. Particular care will be needed if the results of computational modelling are to be used in attempting to relate the haemodynamic environment to the vascular biology, or in determining patient-specific prognoses.

DOI: 10.1002/fld

There is merit and need to perform a benchmark study, for example, comparing MR-acquired data with that obtained by very high definition computed tomography (CT) or with realistic *in vitro* models produced by resin casting or rapid prototyping. This would certainly help to provide more precise error bounds for an individual case; however, it must be appreciated that MR image quality varies from subject to subject, and clearly high definition CT validation could not be performed on each subject. It is conceivable that the process of patient-specific MR image simulation [15] could be used to reduce the uncertainty in determining both the conduit geometry and in relating the computational simulation to *in vivo* data.

For the present, we have concentrated on existing methodologies using clinical data, to make this work accessible to the medical community and ready to be incorporated in current clinical studies. Routine clinical application of this work is limited by the computational fluid dynamics run time which requires a few hours on modern 3 GHz dual core workstations, while the reconstruction processes, including the segmentation, reconstruction and characterization routines, take just minutes.

ACKNOWLEDGEMENTS

The authors are grateful to Dr K. L. Lee and Prof. D. Firmin of Imperial College for help with MR data acquisition and support through Imaging Sciences. Partial support for this work was provided by the EU through the Research Training Network 'HaeMOdel' grant HPRN-CT-2002-00270.

REFERENCES

1. Wootton DM, Ku DN. Fluid mechanics of vascular systems diseases and thrombosis. *Annual Review of Biomedical Engineering* 1999; **1**:299–329.
2. Ouriel K. Peripheral arterial disease. *The Lancet* 2001; **358**:1257–1264.
3. Henry M, Rath PC, Klonaris C, Katsargyris A, Henry I, Hugel M. Peripheral vascular diseases: an update on endovascular therapy. *Indian Heart Journal* 2005; **57**:747–766.
4. Caro CG, Fitz-Gerald JM, Schroter RC. Atheroma and arterial wall shear. Observation, correlation and proposal of a shear dependent mass transfer mechanism for atherogenesis. *Proceedings of the Royal Society of London, Series B* 1971; **177**(46):109–159.
5. Fry DL. Acute vascular endothelial changes associated with increased blood velocity gradients. *Circulation Research* 1968; **12**:165–197.
6. Ku DN, Giddens DP. Pulsatile flow in a model carotid bifurcation. *Arteriosclerosis* 1985; **3**(1):31–39.
7. Gibson CM, Diaz L, Kandarpa K, Sacks FM, Pasternak RC, Sandor T, Feldman C, Stone PH. Relation of vessel wall shear stress to atherosclerosis progression in human coronary arteries. *Arteriosclerosis Thrombosis and Vascular Biology* 1993; **13**:310–315.
8. Younis HF, Kaazempur-Mofrad MR, Chan RC, Isasi AG, Hinton DP, Chan DP, Chau AH, Kim LA, Kamm RD. Hemodynamics and wall mechanics in human carotid bifurcation and its consequences for atherogenesis: investigation of inter-individual variation. *Biomechanics and Modelling in Mechanobiology* 2004; **3**:17–32.
9. Giordana S, Sherwin SJ, Peiró J, Doorly DJ, Crane JS, Lee KE, Cheshire NJ, Caro CG. Local and global geometric influence on steady flow in distal anastomoses of peripheral bypass grafts. *Journal of Biomechanical Engineering* 2005; **127**(7):1087–1098.
10. Giordana S, Sherwin SJ, Peiró J, Doorly DJ, Papaharilaou Y, Caro CG, Watkins N, Cheshire N, Jackson M, Bicknall C, Zervas V. Automated classification of peripheral distal by-pass geometries reconstructed from medical data. *Journal of Biomechanics* 2005; **38**(1):47–62.
11. Steinman DA. Image-based computational fluid dynamics modelling in realistic arterial geometries. *Annals of Biomedical Engineering* 2002; **40**(4):483–497.
12. Löhner R, Cebral JR, Soto O, Yim P, Burgess JE. Applications of patient-specific CFD in medicine and life sciences. *International Journal for Numerical Methods in Fluids* 2003; **43**:637–650.

DOI: 10.1002/fld

13. Antiga L, Ene-Iordache B, Remuzzi A. Computational geometry for patient-specific reconstruction and meshing of blood vessels from MR and CT angiography. *IEEE Transactions on Medical Imaging* 2003; **22**(5):674–684.
14. Cebral JR, Castro MA, Appanaboyina S, Putman CM, Millan D, Frangi AF. Efficient pipeline for image-based patient-specific analysis of cerebral aneurism hemodynamics: technique and sensitivity. *IEEE Transactions on Medical Imaging* 2005; **344**:457–467.
15. Lee KL, Doorly DJ, Firmin DN. Numerical simulations of phase contrast velocity mapping of complex flows in an anatomically realistic bypass graft geometry. *Medical Physics* 2006; **7**(33):2621–2631.
16. Meyers JG, Moore JA, Ojha M, Johnston KW, Ethier CR. Factors influencing blood flow patterns in the human right coronary artery. *Annals of Biomedical Engineering* 2001; **29**:109–120.
17. Moore JA, Steinman DA, Holdsworth DW, Ethier CR. Accuracy of computational hemodynamics in complex arterial geometries from magnetic resonance imaging. *Annals of Biomedical Engineering* 1999; **27**:32–41.
18. Moore JA, Rutt BK, Karlik SJ, Yin K, Ethier CR. Computational blood flow modeling based on in vivo measurements. *Annals of Biomedical Engineering* 1999; **27**:627–640.
19. Moore JA, Steinman DA, Ethier CR. Computational blood flow modeling: errors associated with reconstructing finite element models from magnetic resonance images. *Journal of Biomechanics* 1998; **31**:179–184.
20. Giordana S. Geometrical reconstruction from medical images, classification and modelling of arterial bypass grafts. *Ph.D. Thesis*, Aeronautics Department, Imperial College London, 2004.
21. Deshpande VS, Shea SM, Laub G, Simonetti OP, Finn JP, Li D. 3D magnetization-prepared true-FISP: a new technique for imaging coronary arteries. *Magnetic Resonance in Medicine* 2001; **46**(3):494–502.
22. Peiró J, Formaggia L, Gazzola M, Radaelli A, Rigamonti V. Shape reconstruction from medical images and quality mesh generation via implicit surfaces. *International Journal for Numerical Methods in Fluids* 2006; **53**(8):1339–1360.
23. Iske A. Optimal distribution of centres for radial basis function methods. *Report TUM-M0004 Technische Universität München* 2000.
24. Turk G, O'Brien JF. Shape transformation using variational implicit functions. *Proceedings of the International Conference on Computer Graphics and Interactive Techniques*, Los Angeles, U.S.A., 1999; 335–342.
25. Carr JC, Fright WR, Beatson RK. Surface interpolation with radial basis functions for medical imaging. *IEEE Transactions on Medical Imaging* 1997; **16**(1):96–107.
26. Buhmann MD. *Radial Basis Functions*: *Theory and Implementations*. Cambridge University Press: Cambridge, U.K., 2003.
27. Turk G, Dinh HQ, O'Brien JF, Yngve G. Implicit surfaces that interpolate. *International Conference on Shape Modeling and Applications*, Genova, Italy, 2001; 62–71.
28. Wahba G. *Spline Models for Observational Data*. SIAM CBMS-NSF Regional Conference Series in Applied Mathematics, vol. 59. SIAM: Philadelphia, PA, 1990.
29. http://www.unchainedgeometry.com/jbloom/misc/polygonizer++.tgz. Last accessed 13 July 2006.
30. Bloomenthal J. *An Implicit Surface Polygonizer. Graphics Gems IV*, vol. 1. Academic Press: New York, 1994; 324–349.
31. Blum H. A transformation for extracting new descriptors of shape. *Models for the Perception of Speech and Visual Form*. MIT Press: Cambridge, MA, 1967; 362–380.
32. Palágyi K, Kuba A. A 3D 6-subiteration thinning algorithm for extracting medial lines. *Pattern Recognition Letters* 1998; **19**:613–627.
33. Kruszyński KJ, van Liere R, Kaandorp J. Quantifying differences in skeletonization algorithms: a case study. *Visualization Imaging and Image Processing* (*VIIP*), Benidorm, Spain, 2005.
34. Lazarus F, Verroust A. Level set diagrams of polyhedral objects. *INRIA Report RR-3546*, 1998.
35. Taubin G. A signal processing approach to fair surface design. *Proceedings of the International Conference on Computer Graphics and Interactive Techniques*, Los Angeles, U.S.A., 1995; 351–358.
36. Desburn M, Meyer M, Schröder P, Barr AH. Implicit fairing of irregular meshes using diffusion and curvature flow. *SIGGRAPH*, Los Angeles, U.S.A., vol. 33, 1999; 317–324.
37. Ohtake Y, Belyaev AG, Bogaevski IA. Polyhedral surface smoothing with simultaneous mesh regularization. *Geometric Modeling and Processing 2000 Theory and Applications*, 2000; 229–237.
38. Tura A. *Vascular Grafts*: *Experiment and Modelling*. Advances in Fluid Mechanics. WIT Press: Southampton, U.K., 2003.
39. *Fluent*: *Flow Modeling Software*. Fluent Inc., Lebanon, U.S.A. Available at: http://www.fluent.com.
40. *TGrid*: *Unstructured Volume Meshing*. Fluent Inc., Lebanon, U.S.A. Available at: http://www.fluent.com.
41. Doorly DJ, Sherwin SJ, Franke PT, Peiró J. Vortical flow structure identification and flow transport in arteries. *Computer Methods in Biomechanics and Biomedical Engineering* 2002; **5**(3):261–275.

DOI: 10.1002/fld